Nanoscale Advances

ROYAL SOCIETY OF CHEMISTRY

PAPER

View Article Online
View Journal | View Issue

Cite this: *Nanoscale Adv.*, 2026, **8**, 260

Enhancement of deep ultraviolet chiral molecular sensing performance by collective lattice resonances of diamond nanostructure arrays

Shengsui Cai,† Jing Wang,†* Wenxuan Liu, Zhaolong Cao, Huanjun Chen, Lei Shao* and Shaozhi Deng

Detecting the circular dichroism (CD) spectra of chiral molecules in the deep ultraviolet (DUV) region is of significant research importance in the biomedical field, as it can reflect not only enantiomer concentration but also molecular structural information. Although low-loss dielectric materials in the ultraviolet region can avoid the photothermal effects of traditional plasmonic materials, their poor electromagnetic field localization limits their application in molecular signal enhancement. Here, we designed a diamond nanostructure array. By exciting the collective lattice resonance (CLR) modes with non-local field distribution characteristics and introducing the coupling between the electric and magnetic CLRs, the optical chirality enhancement in the gap region between the diamond nanostructures is increased to a maximum of more than 150, with an average of over 52 at DUV wavelengths. Such characteristics allow the largely enhanced spatial superposition between the superchiral near field and the target chiral analytes. Moreover, simulation results demonstrate a 22-fold enhancement in the DUV CD signals of chiral molecules, with the enhanced CD intensity exhibiting a linear dependence on molecular concentration. Our results could be potentially used for ultrasensitive detection of chiral biomolecules, which is of interest in biopharmaceutical research applications such as rapid detection of chiral drug molecules at ultra-low concentrations.

Received 11th August 2025
Accepted 10th November 2025

DOI: 10.1039/d5na00768b

rsc.li/nanoscale-advances

Introduction

Chirality describes the geometric properties where an object cannot be superimposed onto its mirror image by rotation or translation. This concept is pivotal across numerous scientific disciplines and holds vital importance in biology and chemistry: the fundamental biomolecules of life (such as L-amino acids and right-handed DNA) are predominantly chiral. Taking proteins as an example, the precise folding of their tertiary structures strictly depends on sequences composed of L-configured amino acids. This perpetuation of chirality underpins the functionality of biomolecules. Consequently, the enantiomer-specific interaction between chiral pharmaceuticals and biomolecules can elicit profoundly different biological effects. A classic case is thalidomide—the (*R*)-enantiomer alleviates morning sickness, while the metabolites of the (*S*)-enantiomer cause severe fetal deformities.[1]

The properties of chiral compounds are dictated by their stereochemistry, making the distinction between enantiomers indispensable in both research and application. Among existing detection techniques, CD spectroscopy characterizes chirality by measuring the differential absorption of left-handed (LCP) and right-handed (RCP) circularly polarized light.[2] Most organic molecules absorb light in the ultraviolet (UV) region due to their electronic transitions, and the absorption bands correspond to specific functional groups. Therefore, CD spectroscopy in the deep-ultraviolet (DUV) region with the wavelength $\lambda < 300$ nm can simultaneously resolve molecular secondary structure[3] and solution purity,[4] offering inherent advantages for trace sample detection. However, the intrinsic chiroptical signal of molecules is exceptionally weak because of the size mismatch between molecules and the wavelength of light, with the difference in absorption between RCP and LCP around 10^{-3} to 10^{-6} times lower than the absolute absorption.[5,6] Besides, conventional optical systems exhibit lower transmittance in the DUV band, and photodetectors show poorer response sensitivity in this spectral region. These factors combine to drastically reduce the signal-to-noise ratio during detection, severely hindering the realization of high-sensitivity chiral detection at low concentrations.

Enhancing the CD signal of chiral molecules is therefore paramount. In recent years, novel nanophotonic materials have emerged that can support superchiral near fields to boost the chiral interaction between light and matter. They can provide

State Key Laboratory of Optoelectronic Materials and Technologies, Guangdong Provincial Key Laboratory of Display Materials and Technologies, School of Electronics and Information Technology, Sun Yat-Sen University, Guangzhou, 510275, China. E-mail: shaolei5@mail.sysu.edu.cn; wangj968@mail.sysu.edu.cn

† These authors contributed equally to this work.

large optical chirality density, C, thereby enabling significant enhancement of molecular CD signals.[7,8] C is defined as follows:

$$C = -\frac{\omega}{2c^2}\mathrm{Im}(\mathbf{E}^* \cdot \mathbf{H}), \quad (1)$$

where C is the speed of light, and ω is the angular frequency of light. $\mathbf{E}$ and $\mathbf{H}$ are the complex electric and magnetic fields, respectively. For LCP and RCP light propagating in free space, $C_{\mathrm{CPL}} = \pm(\varepsilon_0\omega/2c){E_0}^2$, where ε_0, μ_0 and E_0 are the permittivity of free space, permeability of free space and incident electric field amplitude. Therefore, the ratio C/C_{CPL} demonstrates an enhancement in the optical chirality of the nanostructures' nearfield compared to that of circularly polarized light (CPL) propagating in free space. When the locally enlarged electric field and magnetic field spatially overlap and are aligned with a phase difference of $\pm\pi/2$, C is significantly enhanced.[9,10] For practical chiral sensing, nanophotonic structures that can produce a large-area distribution of significantly enlarged C with uniform signs are necessary.

Plasmonic nanostructures can provide strong local field enhancement and have been demonstrated to amplify CD signals of large molecules in the visible–near-infrared range.[11–18] However, it should be noted that in most studies within this spectral band, the resonance wavelengths of plasmonic nanostructures do not cover the absorption features of chiral molecules in the UV region.[19–23] Consequently, their CD enhancement mechanism primarily originates from plasmon-induced CD responses rather than the intrinsic signals of biological chiral molecules that reflect the molecular secondary structures. Furthermore, except for a few metals such as aluminum,[24] most plasmonic materials exhibit high ohmic losses at the absorption peaks of small chiral molecules at DUV wavelengths, limiting their applicability in biosensing.

In contrast to plasmonic metallic materials, high-refractive-index dielectric nanostructures (*e.g.*, silicon nitride, diamond, and silicon) simultaneously support both electric and magnetic Mie resonance modes.[9,10,25–28] Through the involvement of mechanisms such as intermodal coupling or excitation of dark modes, these structures can achieve high optical chirality enhancement with uniform handedness within their internal regions.[10,27,28] Diamond, in particular, stands out as a highly promising material. The growth and etching techniques of diamond film have achieved great advances recently.[29] The extremely low optical loss of diamond in the DUV regime makes it exceptionally suitable for molecular sensing in such a spectral range.[30] Introducing asymmetry into diamond cylindrical arrays has been numerically shown to enable optical chirality enhancement factors up to 1100 in the deep ultraviolet.[9] This ultrahigh optical chirality significantly enhances the structure's efficacy for enantiomer examination. However, strong optical chirality enhancement supported by diamond and other high-index dielectric nanostructures is predominantly confined in their internal volumes. This restricts the effectiveness of superchiral nearfield in regions outside the nanostructures where molecules interact, which is crucial for sensing applications. Additionally, practical implementation requires careful consideration of micro/nanofabrication feasibility and experimental constraints to ensure the designed structures are viable for real-world use.

Herein, we designed a single-period square lattice array of diamond nanodisks that will not bring about significant challenges in nanofabrication. By spectrally overlapping two distinct collective lattice resonance (CLR) modes to maximize their coupling through tuning the structure's geometric parameters, we demonstrated numerically significant optical chirality enhancement in the external proximity of the diamond nanostructures at DUV wavelengths. The in-plane nonlocal nature of concentrated electromagnetic fields of CLR modes modulates the concentration of the local density of optical chirality, shifting its spatial distribution with large C enhancement from the interior of the nanostructures to the interstitial spaces between them. The C enhancement in the in-plane nonstructural region of the diamond nanodisk lattice reaches a maximum of over 150, with an average of over 52 at the CLR resonance wavelength, which we can readily tune through structural parameter adjustment. We further performed simulations to calculate the performance improvement of the diamond nanodisk array brought into the practical CD measurements. Our results show that a 100-nm-thick chiral molecule film coated on a square lattice array (lattice constant = 160 nm) of diamond nanodisks (diameter = 121 nm, height = 52 nm) exhibited 22 times stronger CD peak signals than the control film without any nanostructures in the DUV region. Thus, our diamond nanostructure array architecture delivers much stronger and more accessible optical chirality enhancement, making it highly suitable for real-world sensing scenarios. These findings hold significant potential for detecting biomolecular chirality, with critical implications for applications such as drug development.

Results and discussion

To quantitatively evaluate the impact of CLRs within diamond nanostructure lattice arrays and reveal their underlying mechanism in improving the chiroptical nearfield surrounding the nanostructure, we first selected diamond nanospheres and their lattice arrays as simple model systems. We conducted finite element method-based numerical simulations on a diamond nanosphere with a diameter of $d = 120$ nm and an infinitely periodic square lattice array of it (Fig. 1a and b), using the general-purpose commercial software COMSOL (see Methods in the SI). The refractive index of the surrounding medium was set at $n_{\mathrm{bg}} = 1.46$ to mimic the effect of commonly employed substrates and solutions in experiments, as we will present in this work. The refractive index and extinction coefficient of diamond were extracted from ref. 30. The lattice constant of the periodic array was set at $a = 154$ nm. The array exhibits C4 rotational symmetry, ensuring isotropic optical responses. Circularly polarized light was incident along the z-axis (Fig. 1a).

Comparative studies revealed significant differences between the isolated diamond nanosphere and its periodic arrays. The simulation-calculated scattering cross-section spectrum of the isolated diamond nanosphere agrees perfectly with that predicted from Mie theory. We further utilized Mie

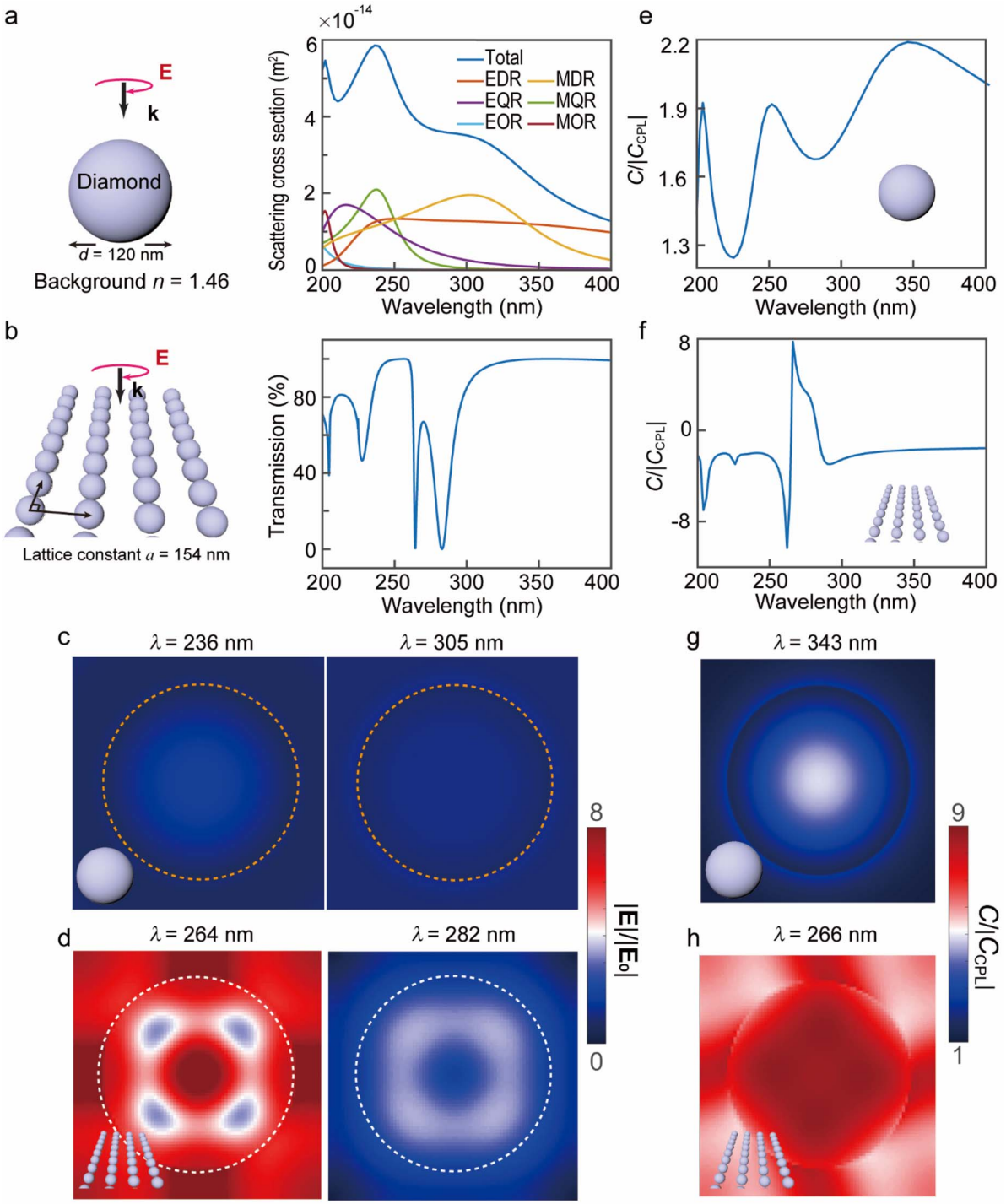

Fig. 1 Superchiral near field boosted by collective lattice resonances in a diamond nanosphere lattice. (a) Schematics of an isolated single diamond nanosphere in a surrounding medium with background refractive index $n = 1.46$ (left). The scattering spectrum and multipole analysis of the diamond nanosphere calculated from Mie theory (right). We calculated the contribution from electric dipole resonance (EDR), magnetic dipole resonance (MDR), electric quadrupole resonance (EQR), magnetic quadrupole resonance (MQR), electric octupole resonance (EOR), and magnetic octupole resonance (MOR). (b) Schematics of a square array of diamond nanospheres in a surrounding medium with $n = 1.46$ (left) and its transmission spectrum (right). (c) E field enhancement and current vectors of the isolated diamond nanosphere at $\lambda = 236$ nm and $\lambda = 305$ nm. (d) E field enhancement and current vectors of a single diamond nanosphere in the lattice at $\lambda = 264$ nm and $\lambda = 282$ nm. (e and f) Averaged C enhancement spectra in the non-structural area for the isolated diamond nanosphere and the sphere array. (g and h) Spatial distributions of the C enhancements for the isolated single diamond nanosphere at $\lambda = 343$ nm and the diamond nanosphere in the lattice at $\lambda = 266$ nm.

theory to analyse the contributions from different multipolar resonance modes to the scattering of the isolated nanosphere (Fig. 1a). The mode analysis shows that the broad strongest scattering peak centred at 236 nm results from the excitation of multiple resonance modes including electric dipole resonance (EDR), magnetic dipole resonance (MDR), magnetic quadrupole resonance (MQR), and magnetic octupole resonance (MOR). The MQR mode plays the most important role. In contrast, the scattering peak centred at 305 nm is dominated by the EDR and MDR modes. The scattering peak centred at 202 nm results from the excitation of MDR, MQR, MOR, electric quadrupole resonance (EQR), and electric octupole resonance (EOR), with the MOR dominating. We then constructed an infinitely sized square lattice array of the diamond nanosphere with the same size. The transmission spectrum of the array displayed an asymmetric line shape (Fig. 1b). A Rayleigh Anomaly (RA) at 225 nm ($\lambda_{RA} = a \cdot n_{bg}$) suppresses higher-order Mie resonances,[31,32] leading to the disappearance of the original resonance near 236 nm. CLR modes emerged in the proximity of the RA. The narrow-linewidth (~3 nm) transmission dip at 264 nm corresponds to the electric dipole CLR (ED-CLR), while the transmission dip at 282 nm corresponds to the magnetic dipole CLR (MD-CLR) (Fig. 1b), similar to the result reported for periodic Si nanosphere arrays.[33] The excitation of the CLR modes results in a much more remarkably enhanced electric field (Fig. 1c and d) because of their higher quality factor. The CLR resonances also exhibit an in-plane non-local nature, with their enhanced electromagnetic field extended to non-structural interstitial spaces between the unit nanospheres.

We then studied the optical chirality enhancement ($C/|C_{CPL}|$) properties of both the isolated diamond nanosphere and its lattice array. We first calculated the average value of $C/|C_{CPL}|$ of the non-structural region over an area of $a \times a$ in the horizontal central plane of the nanostructures as a function of wavelength (Fig. 1e and f). The diamond nanosphere was placed in the centre of the square. The spectra of averaged $C/|C_{CPL}|$ display distinct peaks, with wavelengths differing from those of the corresponding scattering spectra. For the isolated diamond nanosphere, the averaged $C/|C_{CPL}|$ reaches its peaks at 204, 250, and 343 nm (Fig. 1e), where the EQR and MOR, EDR and MDR or MQR, and EDR and MDR share the same contribution to scattering, respectively. Similarly, for the diamond nanosphere array, the averaged $C/|C_{CPL}|$ reaches its peak at 266 nm, which is remarkably close to the transmission peak in between the ED-CLR and MD-CLR modes (Fig. 2f). A sign reversal in $C/|C_{CPL}|$ was observed because of the abrupt phase shifts between narrow ED-CLR and MD-CLR at varying wavelengths. Both results imply the importance of interaction between electric and magnetic resonances in generating superchiral near fields. The spectral overlapping between the electric and magnetic optical modes greatly affects the density of the optical chirality. Our results clearly revealed that the excitation of CLRs enables a large enhancement of the optical chirality, with the largest averaged $C/|C_{CPL}|$ at non-structural area increasing from 2.2 to 8. We further plot the spatial distributions of $C/|C_{CPL}|$ at the wavelengths where it reaches its maximum, *i.e.* 343 nm for the isolated nanosphere and 266 nm for its lattice (Fig. 1g and h). In both cases, the strong optical chirality results from the coupling between electric and magnetic dipolar resonances, which are EDR–MDR coupling for the isolated nanosphere and (ED-CLR)–(MD-CLR) coupling for the nanosphere lattice. The EDR–MDR coupling is weak for an isolated nanosphere, with the superchiral near field primarily confined to the central region inside the nanosphere (Fig. 1e–g). In contrast, (ED-CLR)–(MD-CLR) coupling is much stronger, and the resulting superchiral near field maintains a large concentration in the non-structural area in between the spheres (Fig. 1f–h). Such characteristics are critical for enhancing chiral optical signals in practical applications.

We have not achieved a perfect spectral overlap between the ED-CLR and MD-CLR modes in the nanosphere lattice. Due to the inherent symmetry of the dielectric nanospheres and the resulting poor tunability in their resonance frequencies, it is extremely challenging to tune the geometric parameters of the nanosphere lattice to precisely adjust the ED-CLR and MD-CLR resonances at the same wavelength. The spectral separation of the ED-CLR and MD-CLR modes in symmetric arrays (the lattice constants along x and y direction $a_x = a_y$) of nanospheres can be resolved *via* asymmetric designs (*e.g.*, $a_x \neq a_y$), as one recent experimental work demonstrates in a Si nanosphere lattice.[34] However, the fabrication of diamond nanospheres with uniform sizes remains challenging. In contrast, nanodisks offer superior manufacturability, and their Mie resonances can be tuned *via* both the size and the diameter-to-height aspect ratio.[10] We therefore replaced the repeating units in the aforementioned periodic array with diamond nanodisks (Fig. 2a), in order to design a diamond nanostructure lattice that balances high optical chirality enhancement, structural fabrication feasibility, and application viability. To systematically investigate the relationship between CLRs and optical chirality enhancement, we conducted parametric studies by varying the array period a from 150 to 170 nm (Fig. 2b and S1) while keeping the disk diameter d and height h fixed at $d = 121$ nm and $h = 51$ nm, respectively. Similar to the periodic diamond nanosphere arrays, we observed the RA at 220–250 nm ($\lambda_{RA} = a \cdot n_{bg}$) suppressing higher-order Mie resonances of individual nanodisks (Fig. S1). We also observed the excitation of ED-CLR and MD-CLR modes, which account for the dips in the transmission spectra of the diamond nanodisk array (Fig. 2b–d and S1). By varying the lattice constants along the x and y directions, a_x and a_y, independently, the two CLRs exhibit distinct periodic dependence (Fig. S2).[32,35] Under the excitation of linearly polarized light with the polarization direction along the x axis, the ED-CLR redshifts while the MD-CLR rarely shifts as a_x increases. In contrast, the MD-CLR redshifts while the ED-CLR rarely shifts as a_y increases. A pronounced transmission peak was observed between the ED-CLR and MD-CLR in the transmission spectra. This peak can approach its highest intensity as the ED-CLR and MD-CLR are well aligned at $a_x = a_y$, suggesting that such a peak arises from the destructive interference between the ED-CLR and MD-CLR modes and can suppress backscattering under Kerker-like conditions (Fig. S2).[32,33,36] In addition, by varying the lattice constant $a = a_x = a_y$, we found

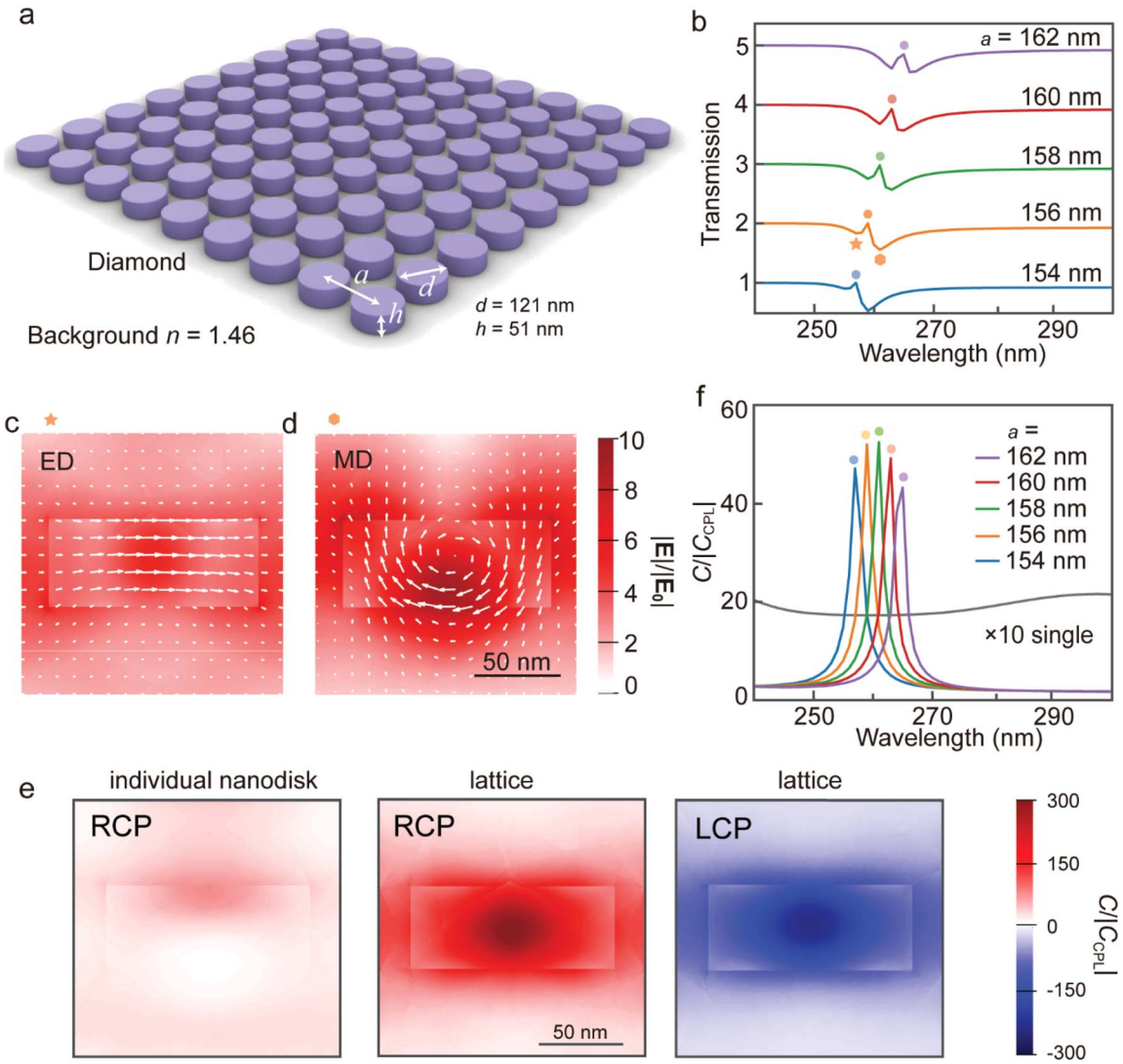

Fig. 2 Superchiral near field boosted by collective lattice resonances in a diamond nanodisk lattice. (a and b) Schematics of square arrays of diamond nanodisks in a surrounding medium with $n = 1.46$ (a) and their transmission spectra (b). The lattice constant of the array a varies from 154 nm to 162 nm. The diameter and height of the nanodisk unit were fixed at 121 nm and 51 nm. (c and d) Distributions of electric field enhancement and current vectors in the central plane perpendicular to the lattice plane showing excitation of the ED-CLR and the MD-CLR modes at $\lambda = 259$ nm and $\lambda = 262$ nm, respectively, for the nanodisk array with $a = 156$ nm. (e) Spatial distributions of $C/|C_{CPL}|$ of an isolated diamond nanodisk control structure at $\lambda = 240$ nm under RCP excitation (left), and a diamond nanodisk in a periodic array with $a = 158$ nm at $\lambda = 262$ nm under RCP excitation (middle) and LCP excitation (right), respectively. (f) Averaged C enhancement spectra of the isolated diamond nanodisk and the nanodisk arrays with different a. The averaged C enhancements were calculated by averaging the value of $C/|C_{CPL}|$ outside the nanodisk over an area of 158 nm × 158 nm (isolated nanodisk) or $a \times a$ (nanodisk arrays) in the horizontal central plane of the nanostructures as a function of wavelength, with the diamond nanodisk placed in the centre.

that the intensity of the peak generated from (ED-CLR)–(MD-CLR) coupling can reach unity at their resonance wavelength.

The in-plane non-local resonance nature of CLR modes enables the distribution of strongly enhanced superchiral near fields beyond the physical boundaries of the diamond nanodisks. The perfect alignment between the ED-CLR and MD-CLR ensures the extremely large local optical chirality in the interstitial spaces between nanodisks. For instance, $C/|C_{CPL}|$ exceeds 150-fold within the gaps at $a = 158$ nm, with its average value in the in-plane non-structural region reaching 52 at the resonance wavelength ($\lambda = 262$ nm), both of which are much larger than that of the isolated diamond nanodisk control structure (Fig. 2e and f). The value of $C/|C_{CPL}|$ can reach up to 300 inside the nanodisk. As predicted, illumination with the opposite handedness of CPL yields results with equal magnitudes but opposite sign (Fig. 2e). The high density of optical chirality in the gap region is highly advantageous for low-concentration chiral molecule detection. We would like to highlight that our symmetric structure enhances the local optical chirality density of the non-structural region by aligning the ED-CLR and MD-CLR modes of the lattice through structure design. It is different from the reported strategy of introducing additional

geometrical anisotropy of the diamond nanostructure metasurface.[9] Moreover, the resonance wavelengths of the CLRs are primarily governed by the periodicity. In principle, the resonance modes can be tuned to any specific wavelengths as long as the material's refractive index permits. Furthermore, this array allows independent modulation of ED-CLR and MD-CLR modes by adjusting a_x and a_y separately, making it highly suitable for designs aiming to maximize C at specific wavelength through ED/MD mode engineering. The enhanced chiral field extends beyond the physical boundaries of the nanostructures, creating more accessible regions for enhancing chiral light–matter interaction. Moreover, the CLR resonance wavelengths can also be tuned by adjusting the nanodisk diameter d (Fig. S3). As the diameter d increases from 50 to 150 nm, the CLR modes exhibit continuous red shifts as well as a reduction in quality factor. We also found that the spatial distribution of the superchiral near field can be regulated by the nanodisk diameter d and the lattice constant a. One can therefore achieve stronger and more extended superchiral near fields by properly designing the structure. In our design, the structural parameters ($d \sim 120$ nm, $h \sim 50$ nm, $a \sim 160$ nm) will not raise significant challenges for the nanofabrication, making the single-period diamond nanodisk array highly suitable as an enhancing substrate platform for the detection of the CD signals of chiral molecules.

To advance toward practical device implementation, we replaced the idealized uniform background with a more realistic material system with an organic molecule, poly(methyl methacrylate) (PMMA), as the surrounding medium and MgF_2 as the substrate (Fig. 3a and b). We chose the PMMA/MgF_2 system because its refractive index profiles closely approximate the homogeneous background conditions in our initial

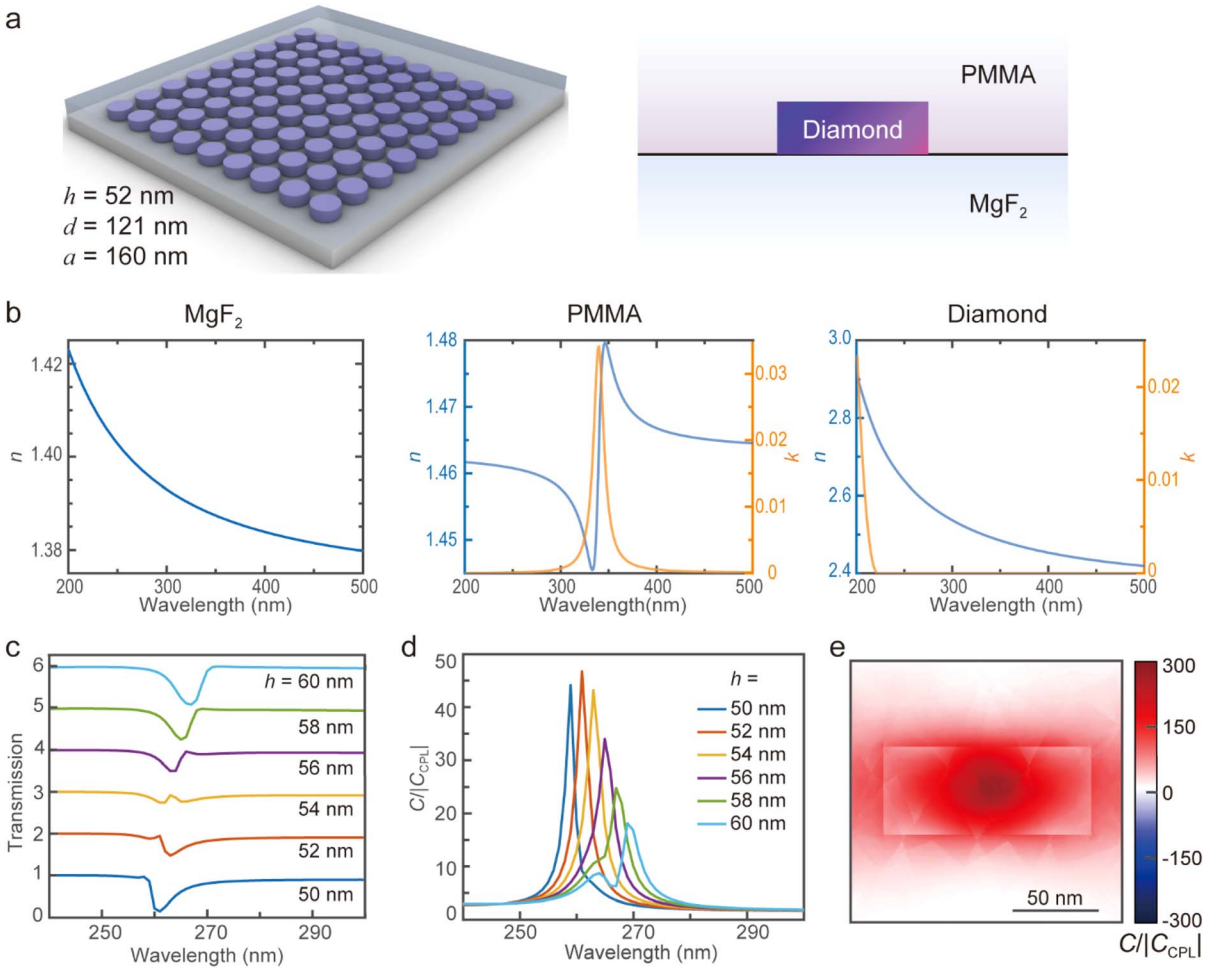

Fig. 3 Superchiral near field enabled by collective lattice resonances in a diamond nanodisk array in an environment mimicking the experimental conditions. (a) Schematics of a square array of diamond nanodisks supported on a MgF_2 substrate and coated with PMMA. (b) Dependence of the refractive index and extinction coefficient dispersion curves of MgF_2, PMMA, and diamond. The data of MgF_2 and diamond were extracted from ref. 32 and 25 respectively. The data of PMMA were obtained from a Lorentzian resonance model by considering the PMMA's absorption at around 320 nm. (c) Transmission spectra of square diamond nanodisk arrays with the lattice constant and the disk diameter fixed at $a = 160$ nm and $d = 121$ nm. The disk height h varied between 50 and 60 nm. (d) Averaged C enhancement spectra of the nanodisk arrays with different h. The averaged C enhancements were calculated by averaging the value of $C/|C_{CPL}|$ outside the nanodisk over an area of $a \times a$ in the horizontal central plane of the nanostructures. (e) Spatial distributions of $C/|C_{CPL}|$ of a diamond nanodisk in a periodic array with $h = 52$ nm at $\lambda = 261$ nm under RCP excitation.

calculations, and the experimental feasibility can be maintained, since MgF_2 has a refractive index close to commonly used organic molecules and exhibits excellent DUV transparency with a negligible extinction coefficient.[37] In our simulation, we modelled PMMA's optical properties with a Lorentzian resonance by considering its ultraviolet absorption (see Methods in the SI).[38] We also provided the complex refractive indices of diamond that we extracted from ref. 25 and employed in our simulation in Fig. 3b for comparison. The primary absorption band of PMMA falls near 320 nm (Fig. 3b), far away from the DUV wavelength range of interest in our study (240–300 nm). This ensures minimal absorption-induced side effects during spectral analysis. Prior studies indicated that the refractive index mismatch suppresses long-range interparticle interactions, consequently inhibiting lattice resonances under normal incidence.[39,40] Introducing the PMMA/MgF_2 system inevitably disrupts the perfect index-matching conditions of our initial design, inducing a slight spectral shift in the CLR modes. In actual fabrication processes, etching-based control over nanostructure height (depth) provides more direct parametric tunability than lithographic regulation of periodicity and diameter in 2D patterning. We therefore systematically adjusted the nanodisk height within the unit cell to parametrically investigate CLR modes and optical chirality enhancement. We set the lattice constant and the disk diameter of the nanodisk array at $a = 160$ nm and $d = 121$ nm, while varying the disk height h between 50 and 60 nm in our simulation (Fig. 3c and d). The calculated performance of the CLRs slightly degrades, as reflected by the less distinct peak and dip features in the transmission spectra (Fig. 3c). Despite this, we can still achieve an alignment between the ED-CLR and the MD-CLR. The largest value of the average $C/|C_{CPL}|$ outside the nanodisk over an area of $a \times a$ in the horizontal central plane of the nanostructures only exhibits a slight decrease from 52 to 47 after taking the real experimental conditions into account (Fig. 3d and e), validating the effectiveness of our structure design.

Our preceding investigations have demonstrated the exceptional DUV optical chirality enhancement capabilities in the non-structural area of periodic diamond nanoarrays. Next, we incorporated chiral molecules into our simulation by blending

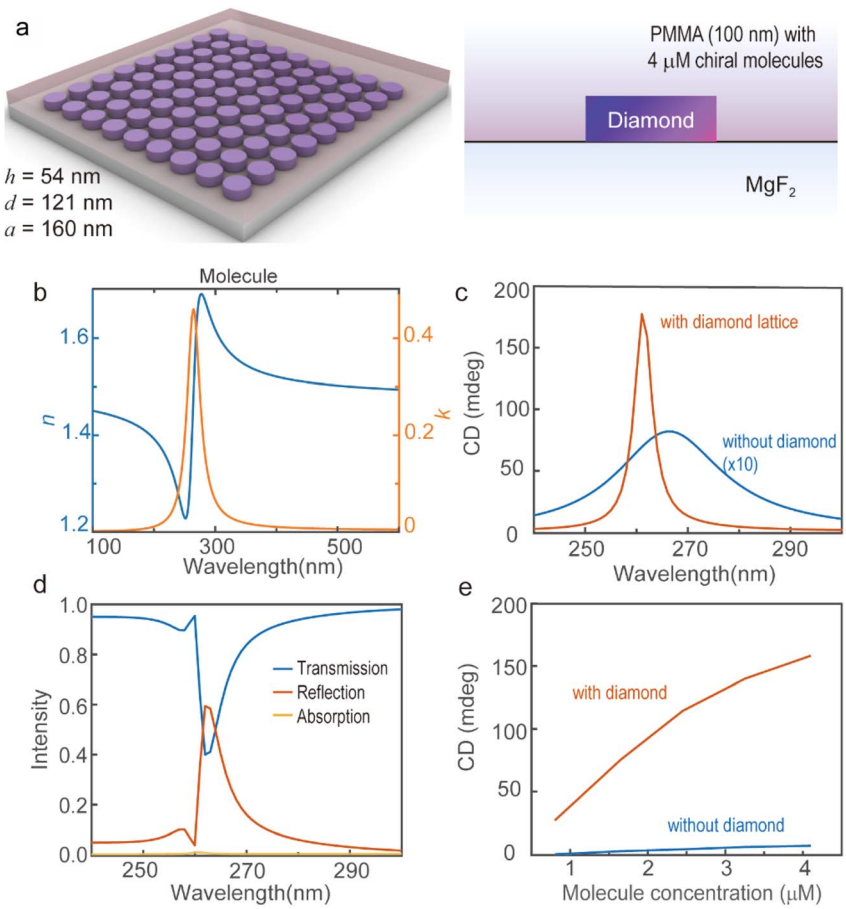

Fig. 4 Improved CD sensing performance by the diamond nanodisk array in an environment mimicking the experimental conditions. (a) Schematics of a diamond nanodisk array coated with the mixture of chiral molecules and PMMA on the MgF_2 substrate. (b) Refractive index and extinction coefficient dispersion curves of the chiral molecule. (c) Calculated CD signals of the chiral molecule–PMMA film with and without the periodic diamond nanodisk array. (d) Transmission, reflection, and absorption spectra of the periodic diamond nanodisk array coated with the chiral molecule–PMMA film. (e) The maximum CD intensities of the periodic diamond nanodisk array coated with the chiral molecule–PMMA film as a function of the molecular concentrations in PMMA.

them with PMMA. We modelled the chiral molecule–PMMA mixture with a 100-nm-thick film to mimic the spin-coating deposited thin layer of chiral molecule samples in sensing experiments (Fig. 4a).[41] To include the chiral optical response of chiral molecules, constitutive equations in the simulation were modified by adding the chiral elements:[42,43]

$$\mathbf{D} = \varepsilon_0 \varepsilon \mathbf{E} - \mathrm{i}\frac{\kappa}{c}\mathbf{H}, \tag{2}$$

$$\mathbf{B} = \mu_0 \mu \mathbf{H} + \mathrm{i}\frac{\kappa}{c}\mathbf{E}, \tag{3}$$

where ε and μ represent the relative permittivity and permeability of materials, respectively. κ is the Pasteur parameter denoting the strength of chirality and is determined by the coupling between the electrical and magnetic responses of the medium. We selected the mixture of surfen and alpha-sulfated cyclodextrins, with a strong CD resonance at ~260 nm,[44] as an example of chiral molecules in the following calculation. We analysed the absorption and CD spectra of the molecule measured by others[44] using Lorentzian fitting[45] to extract the value of its refractive index n, extinction coefficient k, and Pasteur parameterκ (Fig. 4b). n, k, and κ of the chiral molecule are not independent but connected by:[46]

$$\varepsilon = \varepsilon_\mathrm{b} - \gamma\left(\frac{1}{\hbar\omega - \hbar\omega_0 + \mathrm{i}\Gamma} - \frac{1}{\hbar\omega + \hbar\omega_0 + \mathrm{i}\Gamma}\right), \tag{4}$$

$$\kappa = \beta\left(\frac{1}{\hbar\omega - \hbar\omega_0 + \mathrm{i}\Gamma} - \frac{1}{\hbar\omega + \hbar\omega_0 + \mathrm{i}\Gamma}\right), \tag{5}$$

$$\varepsilon = (n + \mathrm{i}k)^2, \tag{6}$$

$$\mu = 1, \tag{7}$$

where ε_b is the background dielectric constant, ω_0 is the molecular optical absorption frequency, and γ and β determine the magnitudes of absorptive and chiral properties, respectively. Γ is the molecular transition damping frequency. We set the value of ω_0 to ensure the chiral molecule exhibits a CD peak at 266 nm. More details of the setting can be found in Methods in the SI. Since we were investigating the chiral optical response induced by the chiral molecules with a very low concentration ($\leq$4 μM) in the PMMA matrix, the effective refractive index and extinction coefficient of the mixture film are almost the same as those of the pure PMMA, as revealed by their calculation according to the chiral molecule–PMMA mass ratio. κ of the mixture film with different chiral molecule concentrations was calculated by assuming it is proportional to the molecule concentration in the mixture.

We then calculated the optical properties of the chiral molecule–PMMA film deposited on MgF_2 with and without diamond nanostructures under the illumination of CPL with different handedness. We obtained the CD signal by calculating the degree of ellipticity:

$$\mathrm{CD}\ (\mathrm{deg.}) = \Delta A \times \ln 10 \times \frac{180}{4\pi} = \ln\left(\frac{T^+}{T^-}\right) \times \frac{180}{4\pi}, \tag{8}$$

where T^+ and T^- are the transmission of the sample under RCP and LCP illuminations, respectively. ΔA corresponds to the absorbance difference for RCP and LCP light. In the absence of any diamond nanostructures, the COMSOL-calculated CD spectrum of the chiral molecule–PMMA film with the chiral molecule concentration of 4 μM perfectly reproduces the result given by the following analytical expression for the CD response:

$$\mathrm{CD} = -\tan^{-1}[\tan \mathrm{h}(k_0 w\, \mathrm{Im}\{\kappa\})], \tag{9}$$

where k_0 and w are the vacuum wave vector and the thickness of the molecular film.[47] Both the CD spectra calculated from the analytical model and from the COMSOL simulation are in good agreement with experimental results in ref. 39 (Fig. 4c), with the CD peak of the molecular film at 266 nm less than 10 mdeg. We adjusted the structure parameters of the diamond nanodisk array (a = 160 nm, d = 121 nm, h = 54 nm) to match its CLR wavelength with that of the molecular CD resonance. Because of the small absorption coefficient of the chiral molecule–PMMA mixture, the calculated absorption of the sample with the diamond array is very low (Fig. 4d). The transmission peak (or reflection dip) near 260 nm in the spectrum arises from destructive interference between the ED-CLR and MD-CLR modes, indicating the highest optical chirality enhancement and the resulting highest CD signal at this wavelength (Fig. 4c). With the help of the diamond nanoarray, we observed a remarkable 177 mdeg peak at 260 nm in the CD spectrum, representing a 22-fold enhancement over that of the unstructured control sample. Such a substantial improvement demonstrates the exceptional capability of the CLR resonances supported by the diamond nanostructure array for chiral signal amplification in the DUV regime. We further performed simulations (Fig. 4e) for mixture films with different chiral molecule concentrations (Fig. 4e). The CD peak intensity was nearly proportional to the molecule concentration. This robust performance, achieving consistent 22-fold signal amplification, confirms the reliability of our diamond nanoarray platform for quantitative chiral sensing applications. The linear relationship between concentration and CD intensity makes the diamond metasurface applicable for the detection of enantiomer concentration.

To further illustrate a clear picture of the distribution of the local optical chirality around the diamond nanostructure in the three-dimensional space and therefore understand the interaction between local superchiral near field and the chiral matter in a more straightforward way, we extracted the value of each local $C/|C_\mathrm{CPL}|$ in the space (Fig. 5a–c), where a 100 nm-thick PMMA film embedded with chiral molecules coats the diamond nanostructure. Both the contours of $C/|C_\mathrm{CPL}|$ in the central vertical cross section and the horizontal cross sections at different heights z of the sample were provided at λ = 260 nm (Fig. 5b and c). Our results clearly revealed that excitation of coupled CLRs of the nanodisk array not only largely increases the superchiral near fields in the in-plane non-structural area, but it also increases the superchiral near fields in the space above the array. The averaged in-plane non-structural $C/|C_\mathrm{CPL}|$

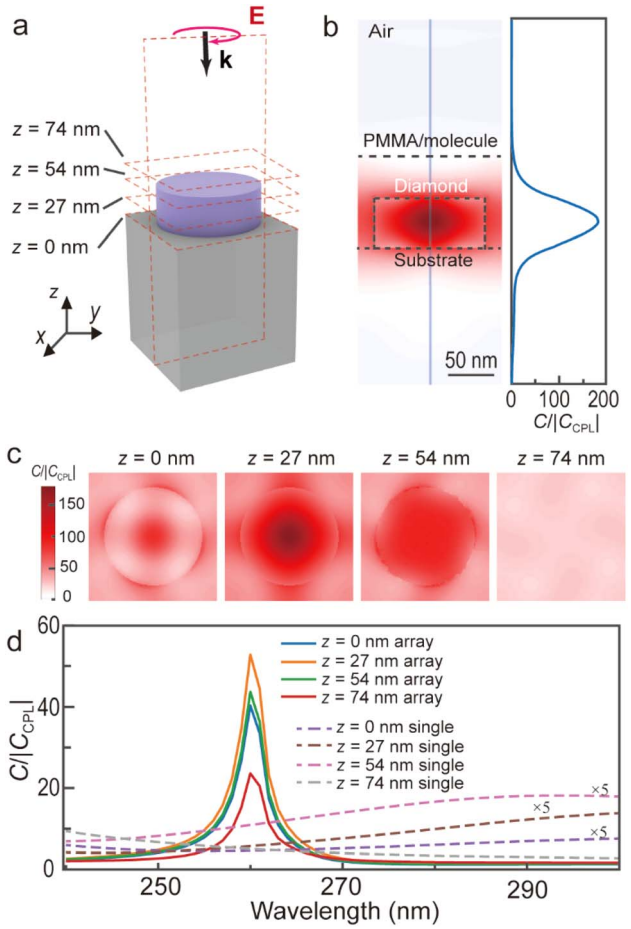

Fig. 5 Distribution of the local optical chirality around the diamond nanostructure under RCP excitation in the three-dimensional space. (a) Schematics of different cross sections of the diamond nanodisk. (b) The x–z vertical cross section of the structure and the corresponding spatial distributions of $C/|C_{CPL}|$ at $\lambda = 260$ nm. (c) The x–y horizontal cross sections of the spatial distributions of $C/|C_{CPL}|$ at $z = 0$ nm (disk bottom), 27 nm (disk centre), 54 nm (disk top), 74 nm, respectively, at $\lambda = 260$ nm. (d) Comparison between averaged C enhancement spectra of the diamond nanodisk and its array at $z = 0$, 27, 54, and 74 nm, respectively. The averaged C enhancements were calculated by averaging the value of $C/|C_{CPL}|$ outside the nanodisk over an area of $a \times a$ in the horizontal central planes of the nanostructures.

reaches as high as 25 even at the site 20 nm above the nanodisk array, *i.e.* $z = 74$ nm (Fig. 5d). Such 3D non-local distribution of strongly enhanced superchiral nearfield is critical for enabling effective interaction between the chiral near field and target chiral molecules. Comparative analysis between periodic arrays and single particle structures, performed after coating with the PMMA–molecule composite solution, revealed distinctly different enhancement characteristics. Compared with the periodic arrays, the isolated diamond nanodisk only produces weak, broadband enhancement outside the nanostructure. This striking difference originates from the coupling between the high-quality-factor CLRs in periodic arrays, which generates sharp, narrowband C enhancement peaks compared to the weak, broadband response of isolated particles.

Conclusions

In summary, through structural design, we have increased the maximum optical chirality enhancement factor $C/|C_{CPL}|$ in the gap region of the diamond array to 150, and the average value of $C/|C_{CPL}|$ in the in-plane non-structural region can reach above 52. The chiral optical enhancement outside the dielectric nanostructure results from the coupling between electric and magnetic CLRs in the diamond lattice. The excitation of CLRs leads to a non-local field enhancement, which enables a greater number of chiral molecules to interact effectively with superchiral regions possessing largely enhanced optical chirality density, giving rise to significantly enhanced chiral optical response of the target chiral molecules. By changing the periodic parameters, the nanostructure array can achieve non-local chiral optical enhancement at specific wavelengths. Our design, based on the excitation of the ED-CLR and MD-CLR modes in the periodic array and boosting their coupling through structure parameter tuning, effectively extends the local superchiral nearfields of the low-loss dielectric structure at DUV wavelengths—fields that are usually confined inside the material—to the area outside the structure. Compared with other diamond nanostructure-based strategies employing periodic structures or asymmetric lattices,[9] our design enables the generation of non-structural superchiral near fields with improved optical chirality enhancement of up to 150, without introducing any structural complexity. Such performance improvement is achieved through the mechanism of bringing effective coupling between ED-CLR and MD-CLR modes. Furthermore, considering the actual application scenarios and the requirements of refractive index matching to excite CLRs, we selected PMMA and MgF_2 as the 'solvent' for chiral molecules and the substrate supporting diamond nanostructures. Our calculation shows that the diamond nanodisk array can amplify the CD signal of a commonly used chiral molecule, sulfated cyclodextrin, in the DUV region by a factor of 22. The peak intensity of the enhanced CD shows a proportional dependence on the concentration of chiral molecules. To summarize, our results provide a powerful solution enabling much stronger and more accessible optical chirality enhancement for chiral sensing. The structural parameters suggested by our calculation will not raise significant challenges in nanofabrication, making the proposed single-period diamond nanostructure array highly suitable as an enhancing substrate for detecting CD signals of chiral molecules. Our results should work for any refractive index-matched surrounding medium (solvents) and substrates, which allows the selection of a suitable solvent to expand our proposed chiral sensing strategy for diverse analytes. In real experiments, one should note that the chiral optical response of the molecules may be influenced by factors other than the designed optical enhancement. For example, the solvent polarity strongly determines the chiral optical signals of the chiral molecules, because it significantly alters the microenvironment of the embedded chiral molecules.[48] Chiral molecules embedded in PMMA with moderate polarity and dissolved in solvents with high polarity such as water and dimethyl sulfoxide

(DMSO) may exhibit original CD signals with varying intensity, peak position, and line shape. As a result, one should pay attention to the specific chemical environment when making comparisons. Moreover, diamond film's inherent absorption becomes remarkable at wavelengths below 230 nm and would degrade the performance of chiral sensing, constraining the extension of our strategy to shorter wavelengths. Nonetheless, we believe that by carefully designing the experiments, our results could boost the development of DUV nanophotonic technologies for real-world chiral sensing scenarios that are critical in applications such as biomolecular chirality analysis, enantiomer examinations, and drug development.

Author contributions

Shengsui Cai: simulation, data curation, and writing–original draft. Jing Wang: conceptualization, formal analysis, data curation, and writing–review & editing. Wenxuan Liu: writing – review & editing. Zhaolong Cao: conceptualization. Huanjun Chen: conceptualization. Lei Shao: conceptualization, resources, supervision, and writing–review & editing. Shaozhi Deng: conceptualization, resources, and writing–review.

Conflicts of interest

There are no conflicts to declare.

Data availability

The data supporting this article have been included as part of the supplementary information (SI). Supplementary information is available. See DOI: https://doi.org/10.1039/d5na00768b.

Acknowledgements

This work was supported by the National Natural Science Foundation of China (Grant No. 2024YFA1209003, 62375290, 12088101, 62411560271), the Pearl River Talent Recruitment Program (Grant No. 2019QN01C216), and the Science and Technology Planning Project of Guangdong Province (2023B1212060025). The authors thank Prof. Zhiqin Chu from the University of Hong Kong for valuable discussions.

Notes and references

1 J. A. Schellman, *Chem. Rev.*, 1975, **75**, 323–331.
2 L. D. Barron, in *Molecular Light Scattering and Optical Activity*, Cambridge University Press, 2004, pp. 123–169.
3 O. O. Oshokoya, C. A. Roach and R. D. JiJi, *Anal. Methods*, 2014, **6**, 1691–1699.
4 X. Lu, J. Tang, X. Dang, X. Jing, K. Xu, H. Li and B. Liang, *RSC Adv.*, 2017, **7**, 13552–13560.
5 S. R. Martin and M. J. Schilstra, in *Biophysical Tools for Biologists, Volume One: In Vitro Techniques*, Academic Press, 2008, vol. 84, pp. 263–293.
6 *Circular Dichroism and the Conformational Analysis of Biomolecules*, ed. G. D. Fasman, Springer US, Boston, MA, 1996.
7 Y. Tang and A. E. Cohen, *Phys. Rev. Lett.*, 2010, **104**, 163901.
8 Y. Tang and A. E. Cohen, *Science*, 2011, **332**, 333–336.
9 J. Hu, M. Lawrence and J. A. Dionne, *ACS Photonics*, 2020, **7**, 36–42.
10 M. L. Solomon, J. Hu, M. Lawrence, A. García-Etxarri and J. A. Dionne, *ACS Photonics*, 2019, **6**, 43–49.
11 M. Schäferling, in *Chiral Nanophotonics: Chiral Optical Properties of Plasmonic Systems*, Springer International Publishing, Cham, 2017, pp. 5–42.
12 M. Hentschel, M. Schäferling, X. Duan, H. Giessen and N. Liu, *Sci. Adv.*, 2017, **3**, e1602735.
13 M. J. Urban, C. Shen, X.-T. Kong, C. Zhu, A. O. Govorov, Q. Wang, M. Hentschel and N. Liu, *Annu. Rev. Phys. Chem.*, 2019, **70**, 275–299.
14 T. Cao, Y. Li, X. Zhang and Y. Zou, *Photon. Res.*, 2017, **5**, 441–449.
15 T. Cao, Y. Li, C.-W. Wei and Y. Qiu, *Opt. Express*, 2017, **25**, 9911–9925.
16 L. Mao, K. Liu, S. Zhang and T. Cao, *ACS Photonics*, 2019, **7**, 375.
17 T. Cao, L. Mao, H. Fan, M. Lian, J. Jia, Y. Su and H. Ren, *Adv. Opt. Mater.*, 2023, **11**, 2202239.
18 M. Cen, J. Wang, J. Liu, H. He, K. Li, W. Cai, T. Cao and Y. J. Liu, *Adv. Mater.*, 2023, **34**, 2270263.
19 M. Schäferling, D. Dregely, M. Hentschel and H. Giessen, *Phys. Rev. X*, 2012, **2**, 031010.
20 M. Schäferling, X. Yin, N. Engheta and H. Giessen, *ACS Photonics*, 2014, **1**, 530–537.
21 E. Hendry, R. V. Mikhaylovskiy, L. D. Barron, M. Kadodwala and T. J. Davis, *Nano Lett.*, 2012, **12**, 3640–3644.
22 T. J. Davis and E. Hendry, *Phys. Rev. B: Condens. Matter Mater. Phys.*, 2013, **87**, 085405.
23 S. Lee, S. Yoo and Q. H. Park, *ACS Photonics*, 2017, **4**, 2047–2052.
24 L. V. Besteiro, H. Zhang, J. Plain, G. Markovich, Z. Wang and A. O. Govorov, *Adv. Opt. Mater.*, 2017, **5**, 1700069.
25 W. Zhang, T. Wu, R. Wang and X. Zhang, *Nanoscale*, 2017, **9**, 5701–5707.
26 C. S. Ho, A. Garcia-Etxarri, Y. Zhao and J. Dionne, *ACS Photonics*, 2017, **4**, 197–203.
27 O. Yavas, M. Svedendahl and R. Quidant, *ACS Nano*, 2019, **13**, 4582–4588.
28 J. García-Guirado, M. Svedendahl, J. Puigdollers and R. Quidant, *Nano Lett.*, 2020, **20**, 585–591.
29 J. Jing, F. Sun, Z. Wang, L. Ma, Y. Luo, Z. Du, T. Zhang, Y. Wang, F. Xu, T. Zhang, C. Chen, X. Ma, Y. He, Y. Zhu, H. Sun, X. Wang, Y. Zhou, J. K. H. Tsoi, J. Wrachtrup, N. Wong, C. Li, D. K. Ki, Q. Wang, K. H. Li, Y. Lin and Z. Chu, *Nature*, 2024, **636**, 627–634.
30 H. R. Phillip and E. A. Taft, *Phys. Rev.*, 1964, **136**, A1445–A1448.
31 J. H. Yang, V. E. Babicheva, M. W. Yu, T. C. Lu, T. R. Lin and K. P. Chen, *ACS Nano*, 2020, **14**, 5678–5685.

32 V. E. Babicheva and A. B. Evlyukhin, *J. Appl. Phys.*, 2021, **129**, 040902.
33 V. E. Babicheva and A. B. Evlyukhin, *Laser Photonics Rev.*, 2017, **11**, 1700132.
34 Y. Hu, P. T. Probst, M. K. Habil, H. Sugimoto and M. Fujii, *Adv. Opt. Mater.*, 2025, 01013.
35 S. S. Wang and R. Magnusson, *Appl. Opt.*, 1993, **32**, 2606.
36 G. W. Castellanos, P. Bai and J. Gómez Rivas, *J. Appl. Phys.*, 2019, **125**, 213105.
37 H. H. Li, *J. Phys. Chem. Ref. Data*, 1980, **9**, 161–290.
38 I. A. Aljarrah, A. A. Bani-Salameh, A. A. Ahmad, Q. M. Al-Bataineh, A. M. Alsaad, M.-A. H. Al-Akhras and A. Telfah, *Polym. Bull.*, 2023, **80**, 7533–7543.
39 B. Auguié, X. M. Bendaña, W. L. Barnes and F. J. García De Abajo, *Phys. Rev. B: Condens. Matter Mater. Phys.*, 2010, **82**, 155447.
40 A. G. Nikitin, T. Nguyen and H. Dallaporta, *Appl. Phys. Lett.*, 2013, **102**, 221116.
41 E. S. A. Goerlitzer, M. Zapata-Herrera, E. Ponomareva, D. Feller, A. Garcia-Etxarri, M. Karg, J. Aizpurua and N. Vogel, *ACS Photonics*, 2023, **10**, 1821–1831.
42 M. L. Nesterov, X. Yin, M. Schäferling, H. Giessen and T. Weiss, *ACS Photonics*, 2016, **3**, 578–583.
43 N. Engheta and P. Pelet, *Opt. Lett.*, 1989, **14**, 593.
44 F. Zsila, *Biochem. Biophys. Res. Commun.*, 2015, **460**, 863–867.
45 V. V. Klimov, I. V. Zabkov, A. A. Pavlov and D. V. Guzatov, *Opt. Express*, 2014, **22**, 18564.
46 A. O. Govorov and Z. Fan, *ChemPhysChem*, 2012, **13**, 2551–2560.
47 E. Mohammadi, K. L. Tsakmakidis, A. N. Askarpour, P. Dehkhoda, A. Tavakoli and H. Altug, *ACS Photonics*, 2018, **5**, 2669–2675.
48 E. Yashima, N. Ousaka, D. Taura, K. Shimomura, T. Ikai and K. Maeda, *Chem. Rev.*, 2016, **116**, 13752–13990.